Letters

Compact Wireless Power Transfer With Enhanced Misalignment Tolerance via Independent Secondary PWM Control

Xingpeng Yu, *Student Member, IEEE*, Ronghuan Xie, *Graduate Student Member, IEEE*, Yixian Tu, Yizhan Zhuang, *Member, IEEE*, Xiangpeng Cheng, Fanghui Yin, *Member, IEEE*, and Yiming Zhang, *Senior Member, IEEE*

***Abstract*—Improving power density and system integration is a pivotal focus for wireless power transfer (WPT) in portable devices. However, challenges, such as misalignment tolerance and power fluctuation persist. This letter introduces a robust solution utilizing secondary independent PWM control. A coil structure combining solenoids and reverse windings ensures passive misalignment tolerance, while a grooved magnetic core integrates the converter, optimizing compactness. In addition, the secondary PWM control achieves precise output voltage regulation without communication. A high-power-density WPT prototype validates the proposed coupler and control method, demonstrating less than 1% output voltage fluctuation under a 50% misalignment and maintaining over 89% efficiency at 100 W. The secondary device is highly compact, measuring only 60 mm × 30 mm × 7.5 mm and achieving power density of 7.41 W/cm^3.**

***Index Terms*—High power density, misalignment tolerance, receiver control, wireless power transfer (WPT).**

I. INTRODUCTION

WIRELESS power transfer (WPT) has become widely adopted due to its inherent safety, convenience, and reliability [1], [2]. Recent advancements have focused on high-power-density WPT systems for consumer electronics and portable devices. Higher power density facilitates smaller, more compact designs, enabling seamless integration with electronic devices [3]. However, these benefits come with challenges, particularly in misalignment tolerance.

While antimisalignment coil designs, such as double-d (DD) or bipolar (BP) coils [4], [5], can enhance tolerance, their complexity often conflicts with the goal of compact, high-density systems [6], [7]. Traditional designs neglect the placement of converters, resulting in low system integration and increased volume.

Efforts to improve misalignment tolerance through coupler designs have shown limited success, as output voltage deviations persist under varying conditions. Existing solutions, such as additional dc–dc stages [8] or tunable compensation components [9] and [10], add complexity and inefficiency. Secondary active rectifiers with phase shift modulation (PSM) achieve precise voltage regulation without communication [11], [12] but disrupt inverter zero-phase angle (ZPA) operation, reducing efficiency. Similarly, pulse density modulation [13], [14], [15] control suffers from reduced sensitivity and increased voltage ripple.

This letter introduces a compact WPT system with secondary-side independent pulse width modulation (PWM) control. The proposed system combines a robust misalignment-tolerant coupler, featuring solenoid coils, reverse windings, and a grooved magnetic core, with PWM-controlled secondary full-bridge rectifier for precise and communication-free voltage regulation. Experimental results confirm the system's high misalignment tolerance, compactness, and reliable voltage control.

II. COMPACT COUPLER DESIGN

The proposed compact coupler consists of a primary coil, a secondary coil, an auxiliary phase-detection coil, and a grooved magnetic core, as illustrated in Fig. 1(a). A cross-sectional view along the *YOZ*-plane is shown in Fig. 1(b). Both primary and secondary coils employ a multilayer and multiturn solenoid winding technique to maximize magnetic coupling within a limited volume.

While the solenoid structure enhances magnetic field uniformity, considerable fluctuations in mutual inductance persist at different positions. To mitigate this issue, the geometric parameters of the primary coil are optimized, and a small reverse winding is introduced at its center. This modification reduces mutual inductance at aligned positions while enhancing it at misalignment boundary regions, thereby achieving a more uniform mutual inductance distribution.

Finite element analyses (FEA) are conducted to determine the optimal coil configuration. Based on the winding-by-winding

Received 26 March 2025; revised 29 April 2025; accepted 13 May 2025. Date of publication 16 May 2025; date of current version 30 June 2025. This work was supported in part by the National Natural Science Foundation of China under Grant 52107183 and in part by the Natural Science Foundation of Fujian Province under Grant 2022J06011. *(Corresponding authors: Xiangpeng Cheng; Fanghui Yin; Yiming Zhang.)*

Xingpeng Yu, Ronghuan Xie, Yixian Tu, Yizhan Zhuang, Xiangpeng Cheng, and Yiming Zhang are with the School of Electrical Engineering and Automation, Fuzhou University, Fuzhou 350108, China (e-mail: 240110012@fzu.edu.cn; 230127018@fzu.edu.cn; 012101334@fzu.edu.cn; zyz_joe@fzu.edu.cn; cxp@fzu.edu.cn; zym@fzu.edu.cn).

Fanghui Yin is with Shenzhen International Graduate School, Tsinghua University, Shenzhen 518071, China (e-mail: yin.fanghui@sz.tsinghua.edu.cn).

Color versions of one or more figures in this article are available at https://doi.org/10.1109/TPEL.2025.3570846.

Digital Object Identifier 10.1109/TPEL.2025.3570846

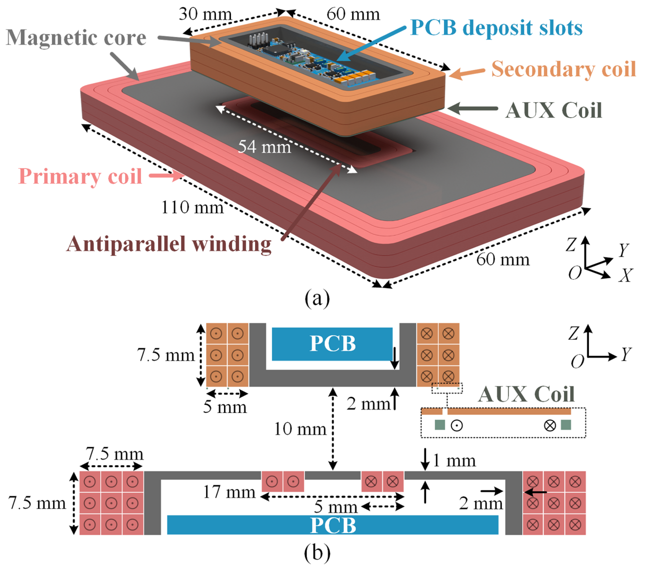

Fig. 1. Compact coupler design. (a) 3-D model. (b) Cross-sectional *YOZ*-plane.

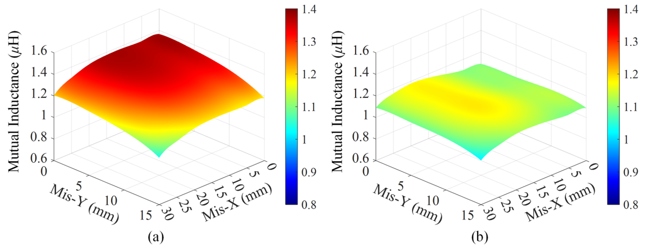

Fig. 2. Variation of mutual inductance with misalignment. (a) Without reverse winding. (b) With reverse winding.

design method proposed in [16], the turns and direction of the outer solenoid coil are fixed, while the turns and axial position of the reverse winding are optimized. The primary coil consists of three layers with a total of nine turns, and the secondary coil comprises three layers with six turns. In addition, a single-layer reverse winding with two turns is embedded within the primary coil and connected in series. To prevent the primary magnetic flux from penetrating the recessed space, a thin layer of magnetic shielding material is positioned behind the reverse winding. As shown in Fig. 2, the mutual inductance variation with and without the reverse winding demonstrates that the ratio between the maximum and minimum mutual inductance across the entire misalignment range is reduced from 1.33 to 1.17.

In addition, a phase-detection auxiliary coil is placed at the base of the secondary coil. Its outer and inner sections are wound in opposite directions to eliminate cross-coupling with the secondary coil. The synchronization process of auxiliary coil will be detailed in Section III.

A grooved ferrite magnetic core is embedded within the solenoid coil, creating a low-reluctance magnetic path and enhancing coupling. The grooved design forms a shielded space within the core for housing the inverter or rectifier.

The geometric parameters of the coupler are listed in Fig. 1. The secondary side is highly compact, with dimensions of

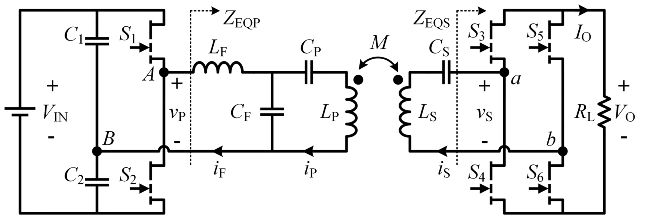

Fig. 3. *LCC*-S compensated WPT topology.

60 mm × 30 mm × 7.5 mm. The FEA results are depicted in Fig. 2, showing stable mutual inductance across a misalignment range up to 50% of the secondary dimensions.

III. TOPOLOGY AND SECONDARY-SIDE PWM CONTROL

The proposed coupler design effectively stabilizes mutual inductance; however, due to inherent parasitic parameters, such as resistance, the implementation of active synchronization control remains essential to ensure precise and controllable output voltage regulation. To address this challenge, a secondary-side PWM-based voltage regulation method is proposed. The following analysis and derivation are conducted using the *LCC*-S topology as a representative example.

A. LCC-S Compensated Topology

The *LCC*-S compensated topology, as illustrated in Fig. 3, consists of a symmetrical half-bridge inverter and an active rectifier. V_{IN} (V_{O}), v_{P} (v_{S}), L_{P} (L_{S}), M, and R_{L} are the primary (secondary) dc voltage, ac voltage, coil self-inductance, mutual inductance, and load resistance. i_{F} is the inverter output current, i_{P} and i_{S} are the primary and secondary coil currents, respectively. Z_{EQP} and Z_{EQS} are the equivalent impedances of the inverter and rectifier, respectively. L_{F}, C_{F}, C_{P}, and C_{S} are the compensation parameters, with their resonant relationship as

$$\omega = 1\Big/\sqrt{L_{\text{F}}C_{\text{F}}} = 1\Big/\sqrt{(L_{\text{P}} - L_{\text{F}})\,C_{\text{P}}} = 1\Big/\sqrt{L_{\text{S}}C_{\text{S}}} \quad (1)$$

where ω is the system operating angular frequency.

Based on first harmonic approximation (FHA) and Kirchhoff's voltage law and neglecting parasitic resistances, the equivalent impedance of the inverter and rectifier are

$$Z_{\text{EQP}} = \frac{8L_{\text{F}}^2}{\pi^2 M^2}R_{\text{L}}, \qquad Z_{\text{EQS}} = \frac{8}{\pi^2}R_{\text{L}}. \quad (2)$$

The dc output voltage is expressed as

$$V_{\text{O}} = \frac{\pi}{2\sqrt{2}}V_{\text{S}(1)} = \frac{M}{2L_{\text{F}}}V_{\text{IN}} \quad (3)$$

where $V_{\text{S}(1)}$ is the fundamental component of v_{s}.

The inverter equivalent impedance remains purely resistive, enabling ZPA operation. The system exhibits load-independent constant-voltage characteristics.

B. Working Principle

The conventional PSM control, such as rectifier internal phase shifting, induces phase changes in the rectifier input voltage

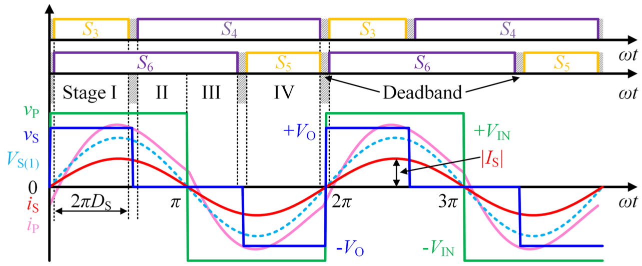

Fig. 4. Key waveforms of proposed PWM control.

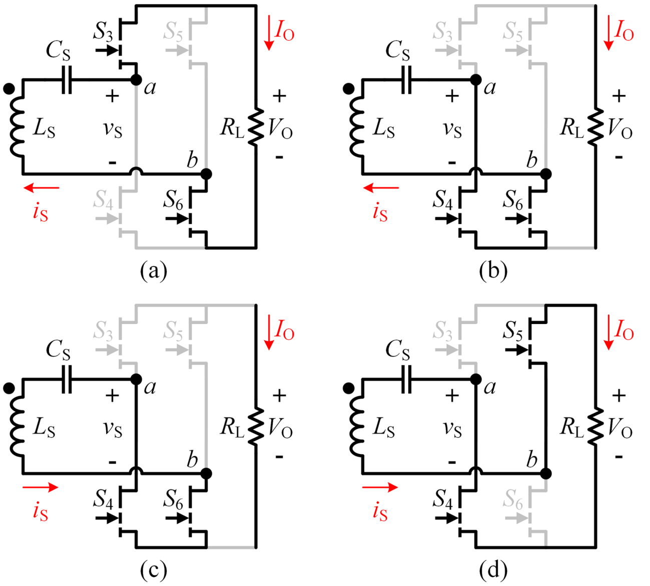

(a) (b) (c) (d)

Fig. 5. Equivalent circuits of active rectifier. (a) Stage I. (b) Stage II. (c) Stage III. (d) Stage IV.

and reactive impedance that disrupts the ZPA operation. This increases switching losses and reduces efficiency.

A secondary-side PWM control method to resolve phase shift issues is introduced. By modulating the duty cycle of the active rectifier, the method creates an odd symmetrical three-level voltage that ensures the phase of the fundamental voltage remains constant while achieving precise output voltage regulation. The key waveforms are illustrated in Fig. 4.

The duty cycle D_S represents the high-level ratio of the rectifier upper switches S_3 and S_5, with complementary PWM signals for the lower switches, where $D_S \leq 0.5$. Each operation cycle is divided into four stages.

Stage I: (0, $2\pi D_S$], S_3, and S_6 conduct, as shown in Fig. 5(a). At the end of Stage IV in the previous cycle, S_4 and S_5 are hard-switching OFF under minimal current. During the subsequent deadband, the coil current i_S transitions from negative to positive, charging the parasitic capacitance (C_{oss3}) of S_3 and discharging the C_{oss6} of S_6, enabling zero-voltage soft-switching of S_3 and S_6. At $2\pi D_S$, the unchanged current direction inhibits the discharge of C_{oss4}, leading to the hard-switching on of S_4.

Stages II and III: ($2\pi D_S$, 2π-$2\pi D_S$], S_4, and S_6 conduct, shown in Fig. 5(b) and (c). The input of rectifier is shorted. At π, current naturally reverses direction. In the deadband around 2π-$2\pi D_S$, S_6 hard-switching on while the coil current i_S remains unchanged, charging the output capacitances C_{oss6} and C_{oss5}, and enabling the soft-switching on of S_5.

Stage IV: (2π-$2\pi D_S$, 2π], S_4, and S_5 conduct, as shown in Fig. 5(d). Coil current i_S power the load. At the end of Stage IV, 2π, $S_{4,}$ and S_5 hard-switching OFF under minimal current, initiating Stage I of the next cycle.

Compared to conventional PSM, which involves up to four hard-switching on events per cycle, this method requires only one hard-switching on event. This significantly reduces switching losses, simplifying control, and improving efficiency.

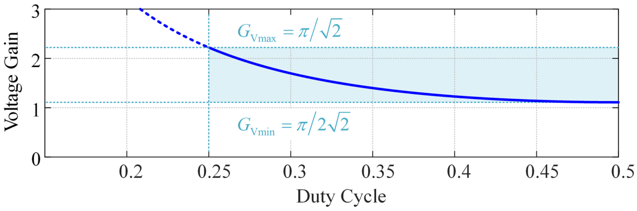

Fig. 6. Variation of G_V with secondary duty cycle D_S.

C. Voltage Gain Analysis

Based on Fig. 4, the input voltage of the rectifier can be derived by FHA as

$$v_{S(1)} = \frac{4V_O \sin^2(\pi D_S)}{\pi} \sin(\omega t). \tag{4}$$

To examine whether the current undergoes a phase shift, the output dc current expression is derived under the assumption that i_S lags the voltage $V_{S(1)}$ by a phase angle θ, namely

$$\begin{aligned} I_O = \frac{1}{2\pi} \Bigg[& \int_0^{\theta} -I_S \sin(\omega t - \theta) d\omega t \\ & + \int_{\theta}^{2\pi D_S} I_S \sin(\omega t - \theta) d\omega t \\ & + \int_{2\pi - 2\pi D_S}^{2\pi} -I_S \sin(\omega t - \theta) d\omega t \Bigg] \\ = & \frac{I_S}{\pi} \left[1 - \cos(2\pi D_S) \cos\theta \right] \end{aligned} \tag{5}$$

where I_S represents the magnitude of the secondary coil current.

Conservation of active power before and after rectifier yields

$$P_{OUT} = V_S I_S \cos(\theta) = V_O I_O. \tag{6}$$

This means the phase angle $\theta = 0$, indicating that $V_{S(1)}$ and I_S are in phase. Z_{EQS} is thus purely resistive, expressed as

$$Z_{EQS} = \frac{V_{S(1)}}{I_S} = \frac{8\sin^4(\pi D_S)}{\pi^2} R_L. \tag{7}$$

The voltage gain of the active rectifier can be defined as

$$G_V = \frac{V_O}{\dot{V}_{S(1)}} = \frac{\pi}{2\sqrt{2}\sin^2(\pi D_S)}. \tag{8}$$

Fig. 6 illustrates the variation of the voltage gain with the duty cycle. By adjusting D_S, the rectifier achieves a wide voltage gain.

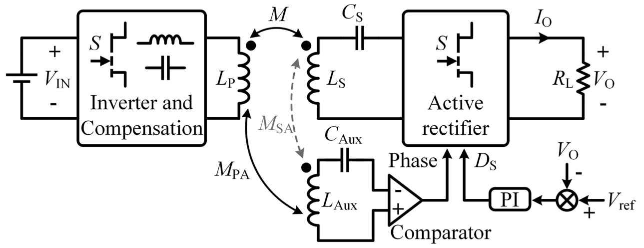

Fig. 7. Block diagram of the secondary PWM control.

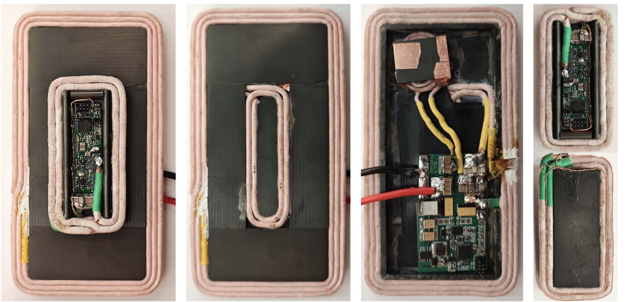
General view
Primary top
Primary bottom
Secondary top and bottom

Fig. 8. Photo of experimental prototype.

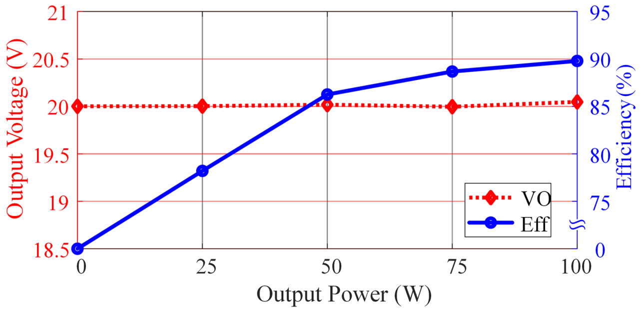

Fig. 9. Experimental results of load regulation.

To ensure efficiency, D_S should be designed within [0.25, 0.5], and G_V within $[\pi/2\sqrt{2}, \pi/\sqrt{2}]$.

D. Synchronization and Control Strategy

Conventional active rectifiers rely on input current phase detection for switching logic, but this method is susceptible to load variations, leading to phase instability under no-load conditions. To ensure a stable primary-side phase reference, an auxiliary phase-detection coil is introduced, decoupled from the secondary coil while maintaining controlled coupling with the primary coil. The induced signal is processed by a zero-crossing comparator to generate a reliable synchronization signal for the active rectifier.

TABLE I
ELECTRICAL PARAMETERS OF THE PROTOTYPE

$C_{1\text{-}2}$	4.7 μF	L_F	3.7 μH
C_F	52.71 nF	C_T	16.62 nF
L_T	15.46 μH	L_R	3.69 μH
C_R	52.88 nF	f	360 kHz

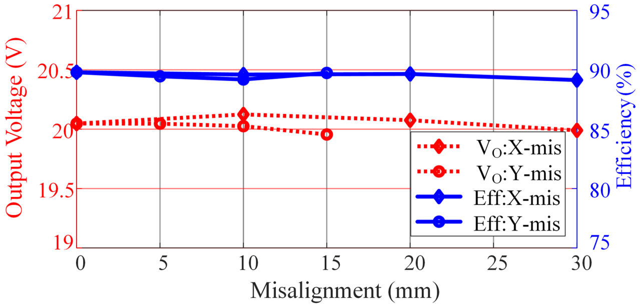

Fig. 10. Experimental results of misalignment.

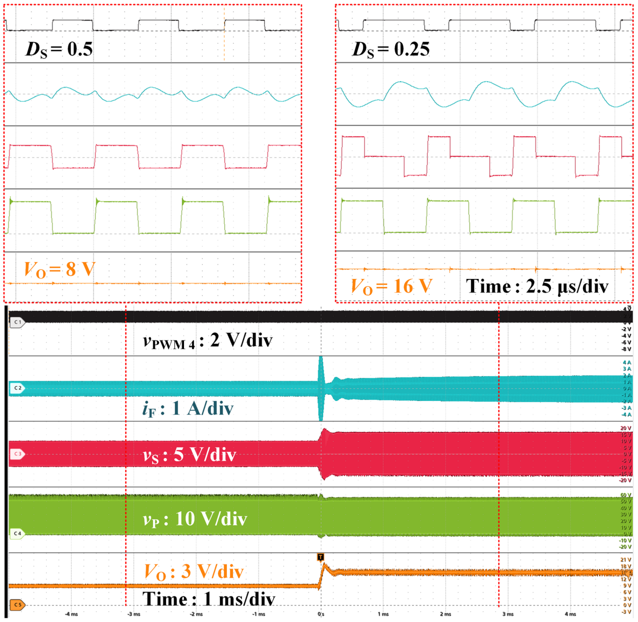

Fig. 11. Dynamic waveforms of duty cycle transition.

The proposed PWM control strategy employs secondary-side closed-loop proportional-integral (PI) regulation to directly adjust the duty cycle, achieving precise output voltage regulation without communication. This framework operates with an open-loop primary side and is particularly suited for single-transmitter, multireceiver systems. The control block diagram of the proposed method is shown in Fig. 7.

IV. EXPERIMENTAL VALIDATION

An experimental prototype is developed based on the geometric parameters in Fig. 1 and shown in Fig. 8, with the parameters summarized in Table I. The compact inverter and rectifier are placed within the grooved magnetic core, and the active rectifier measures only 40 × 11 × 3.5 mm^3.

Under aligned conditions, the experimental results with a 100-V input voltage and a target output voltage of 20 V are shown in Fig. 9. The proposed control method ensures a stable and precise output voltage regulation, achieving a load regulation rate of less than 1%.

At 100-W output power, the misalignment results along the *X*-axis and *Y*-axis are presented in Fig. 10. Across the entire misalignment range, the output voltage fluctuation remains within 1%, and the system maintains a dc–dc efficiency exceeding 89%, demonstrating good misalignment tolerance.

Fig. 11 illustrates the dynamic response to a change in the duty cycle D_{S} from 0.5 to 0.25. Following the transition, the output voltage doubles, verifying the secondary-side independent voltage regulation capability. Meanwhile, the inverter output current phase remains unchanged, maintaining constant ZPA operation. Under the proposed method, the inverter consistently maintains ZPA characteristic regardless of variations in duty cycle or load, which ensures the preservation of zero-voltage-switching (ZVS) operation.

V. CONCLUSION

This letter presents a compact WPT system featuring secondary-side PWM control for precise voltage regulation and robust misalignment tolerance. The innovative coupler design, combining solenoid windings, reverse windings, and grooved magnetic cores, achieves a stable mutual inductance across a wide misalignment range. The integration of compact converters within the magnetic core enhances system power density. The proposed PWM control method enables wide voltage adjustment ranges while preserving ZPA operation on the primary side. Experimental results validate the effectiveness of the coupler design and control method, achieving high performance with minimal voltage fluctuation and high efficiency under misalignment conditions.

REFERENCES

[1] Y. Wu et al., “An integrated charger of wireless power transfer, onboard charger, and auxiliary power module for electric vehicles,” *IEEE Trans. Power Electron.*, vol. 40, no. 4, pp. 6334–6344, Apr. 2025.

[2] E. Rong, P. Sun, G. Yang, J. Xia, Z. Liu, and S. Li, “5-kW, 96.5% efficiency capacitive power transfer system with a five-plate coupler: Design and optimization,” *IEEE Trans. Power Electron.*, vol. 40, no. 1, pp. 2542–2555, Jan. 2025.

[3] S. Li, X. Yu, Y. Yuan, S. Lu, and T. Li, “A novel high-voltage power supply with MHz WPT techniques: Achieving high-efficiency, high-isolation, and high-power-density,” *IEEE Trans. Power Electron.*, vol. 38, no. 12, pp. 14794–14805, Dec. 2023.

[4] Z. Shen, R. Xie, C. Liu, X. Yu, X. Cheng, and Y. Zhang, “An electric vehicle wireless charging system with 400-V and 800-V battery tolerance and strong offset resistance,” *IEEE Trans. Power Electron.*, vol. 40, no. 4, pp. 4722–4726, Apr. 2025.

[5] Y. Zhang, H. Zhou, R. Xie, X. Mao, X. Chen, and Z. Li, “A smooth-output dynamic wireless charging system for automated guided vehicles with dual-receiver magnetic coupler,” *IEEE Trans. Power Electron.*, vol. 40, no. 4, pp. 4711–4715, Apr. 2025.

[6] J. Xiang, C. Q. Jiang, T. Ma, Y. Wang, and Y. Fan, “An ultra-thin self-resonant coupler with nanocrystalline flake ribbons for wireless power transfer system,” *IEEE Trans. Magn.*, vol. 60, no. 9, Sep. 2024, Art. no. 8600805.

[7] L. Zhou, J. Tian, S. Liu, R. Mai, L. Fu, and U. K. Madawala, “High-efficiency WPT systems for potable electronics based on DC-bias-voltage-controlled variable capacitor,” *IEEE Trans. Ind. Electron.*, vol. 71, no. 5, pp. 4707–4718, May 2024.

[8] C. Zhu et al., “Analysis and design of cost-effective WPT systems with dual independently regulatable outputs for automatic guided vehicles,” *IEEE Trans. Power Electron.*, vol. 36, no. 6, pp. 6183–6187, Jun. 2021.

[9] Z. Huang, T. Qin, X. L. Li, L. Ding, H. H.-C. Iu, and C. K. Tse, “Synthesis of inductive power transfer converters with dual immittance networks for inherent CC-to-CV charging profiles,” *IEEE Trans. Power Electron.*, vol. 39, no. 6, pp. 7766–7777, Jun. 2024.

[10] F. Corti et al., “Closed-loop control of inductive WPT system through variable inductor,” *IEEE Open J. Power Electron.*, vol. 5, pp. 1389–1403, 2024.

[11] K. Colak, E. Asa, M. Bojarski, D. Czarkowski, and O. C. Onar, “A novel phase-shift control of semibridgeless active rectifier for wireless power transfer,” *IEEE Trans. Power Electron.*, vol. 30, no. 11, pp. 6288–6297, Nov. 2015.

[12] R. Mai, Y. Liu, Y. Li, P. Yue, G. Cao, and Z. He, “An active-rectifier-based maximum efficiency tracking method using an additional measurement coil for wireless power transfer,” *IEEE Trans. Power Electron.*, vol. 33, no. 1, pp. 716–728, Jan. 2018.

[13] J. Tang, T. Na, and Q. Zhang, “A novel full-bridge step density modulation for wireless power transfer systems,” *IEEE Trans. Power Electron.*, vol. 38, no. 1, pp. 41–45, Jan. 2023.

[14] M. Fan, L. Shi, Z. Yin, L. Jiang, and F. Zhang, “Improved pulse density modulation for semi-bridgeless active rectifier in inductive power transfer system,” *IEEE Trans. Power Electron.*, vol. 34, no. 6, pp. 5893–5902, Jun. 2019.

[15] R. Dai, W. Zhou, Y. Chen, Z. Zhu, and R. Mai, “Pulse density modulation based mutual inductance and load resistance identification method for wireless power transfer system,” *IEEE Trans. Power Electron.*, vol. 37, no. 8, pp. 9933–9943, Aug. 2022.

[16] Y. Zhang, S. Chen, X. Li, and Y. Tang, “Design methodology of free-positioning nonoverlapping wireless charging for consumer electronics based on antiparallel windings,” *IEEE Trans. Ind. Electron.*, vol. 69, no. 1, pp. 825–834, Jan. 2022.